Prominin 1 and Tweety Homology 1 both induce extracellular vesicle formation

Tristan A. Bell[1,2,3]*, Bridget E. Luce[1], Pusparanee Hakim[1], Virly Y. Ananda[1], Hiba Dardari[1], Tran H. Nguyen[1], Arezu Monshizadeh[1], and Luke H. Chao[1,2]*

[1]Department of Molecular Biology, Massachusetts General Hospital, Boston, MA, 02114

[2]Department of Genetics, Blavatnik Institute, Harvard Medical School, Boston, MA, 02115

[3]Current Address: Generate Biomedicines, 101 South St, Somerville, MA, 02143

*For correspondence: Tristan Bell, 185 Cambridge St., CPZN 7250, Boston, MA, 02114, bell@molbio.mgh.harvard.edu; Luke Chao, 185 Cambridge St., CPZN 7250, Boston, MA, 02114, chao@molbio.mgh.harvard.edu.

Running Title: Extracellular vesicle formation in Prominin-family proteins

Keywords: prominin-1, extracellular vesicles, membrane biophysics, protein conformation, cholesterol-binding protein

Preprint Servers: Deposited with bioRxiv under a CC-BY 4.0 license (BIORXIV/2023/566258)

Abstract

Prominin-1 (Prom1) is a five-transmembrane-pass integral membrane protein that associates with curved regions of the plasma membrane. Prom1 interacts with membrane cholesterol and actively remodels the plasma membrane. Membrane bending activity is particularly evident in photoreceptors, where Prom1 loss-of-function mutations cause failure of outer segment homeostasis, leading to cone-rod retinal dystrophy (CRRD). The Tweety Homology (Ttyh) protein family has been proposed to be homologous to Prominin, but it is not known whether Ttyh proteins have an analogous membrane-bending function. Here, we characterize the membrane-bending activity of human Prom1 and Ttyh1 in native bilayer membranes. We find that Prom1 and Ttyh1 both induce formation of extracellular vesicles (EVs) in cultured mammalian cells and that the EVs produced are physically similar. Ttyh1 is more abundant in EV membranes than Prom1 and produces EVs with membranes that are more tubulated than Prom1 EVs. We further show that Prom1 interacts more stably with membrane cholesterol than Ttyh1 and that this may contribute to membrane bending inhibition in Prom1 EVs. Intriguingly, a loss-of-function mutation in Prom1 associated with CRRD induces particularly stable cholesterol binding. These experiments provide

33 mechanistic insight into Prominin function in CRRD and suggest that Prom and Ttyh belong to a single
34 family of functionally related membrane-bending, EV-generating proteins.
35
36 **Introduction**
37 Mammalian cells interact with the extracellular environment through proteins, lipids, and glycans at the
38 plasma membrane. Organized protrusive structures of the membrane such as microvilli and cilia are
39 hotspots for nutrient absorption, cell cycle regulation, and extracellular signaling[1,2]. Membrane
40 protrusions are organized both by interactions with the cytoskeleton and by sorting of proteins and lipids
41 within the membrane bilayer[2–4]. Prominin-1 (Prom1) is a five-transmembrane pass integral membrane
42 protein that interacts with membrane cholesterol at sites of membrane protrusion[5,6]. Prom1 was first
43 characterized as the target of AC133-1, a monoclonal antibody raised against pluripotent human epithelial
44 stem cells[7,8]. Since then, Prom1 has been identified in the apical membranes of most epithelial and
45 neuroepithelial cell types, but is only natively recognized by AC133-1 in stem cells and photoreceptors[9–
46 11]. In photoreceptors, Prom1 associates with a retinal cadherin (Protocadherin-21, Pcdh21) to promote
47 normal outer segment membrane homeostasis[12–14], and several Prom1 mutations are linked to hereditary
48 cone-rod retinal dystrophy (CRRD)[12,15–18]. Most animal genomes also encode at least one paralogous
49 prominin gene (Prominin-2) that is expressed in non-retinal cell types and localizes to positively curved
50 membrane regions[19].
51
52 When overexpressed, Prom1 dramatically reorganizes the plasma membrane of cultured mammalian cells
53 into long protrusions[20,21]. Small-molecule inhibitors of actin and tubulin do not impair the tubulation
54 phenotype, indicating that cytoskeletal interactions are not strictly required for membrane bending[20,21].
55 However, cells treated with cholesterol biosynthesis inhibitors or depletion agents do not exhibit
56 membrane tubulation, suggesting that cholesterol plays a pivotal role in the regulation of Prom1
57 function[20,21].
58
59 Prom1 also induces release of small extracellular vesicles (EVs, < 250 nm in diameter) that bleb from the
60 apical plasma membrane of differentiating epithelial stem cells at organized membrane protrusions such
61 as microvilli and cilia[22–24]. Small Prom1 EVs can be detected in saliva, urine, semen, neural tube fluid, and
62 lacrimal fluid of healthy adults[22,25].
63

64 Recently, the Tweety homology (Ttyh) protein family was hypothesized to be a distant homolog of the
65 prominins[20]. Ttyh proteins share prominins' five-transmembrane topology but have a more minimal
66 extracellular domain[26]. Most animals have three paralogous Ttyh proteins (Ttyh1, Ttyh2, and Ttyh3)[27] that
67 all are predominantly expressed in neural tissues[28–33]. Notably, overexpression of Ttyh1 at the plasma
68 membrane in cultured cells induces plasma membrane tubulation that is strikingly similar to that observed
69 with Prom1[27,34–36].
70
71 Defining mechanisms of membrane bending by Prominin-family proteins is foundational for
72 understanding retinal disease and stem cell development. Here, we reconstitute EV formation by Prom1
73 and Ttyh1 to characterize their functions in a native membrane bilayer system. To our knowledge, we
74 present the first evidence that Ttyh1 induces formation of EVs that are functionally and physically
75 analogous to Prom1 EVs. Ttyh1 EVs are more tubulated and protein-rich than Prom1 EVs. Prom1 forms a
76 more stable interaction with cholesterol than Ttyh1, and when depleted of cholesterol, Prom1 EVs mimic
77 the tubulation observed in Ttyh1 EVs. A CRRD-associated Prom1 mutant (W795R) binds cholesterol more
78 stably than wild-type protein, suggesting that a less dynamic interaction between Prom1 and cholesterol
79 inhibits membrane bending. These findings contribute to a path toward mechanistic understanding of
80 Prominin-family protein function in different tissues, including the role of Prom1 in retinal pathology.
81
82
83 **Results**
84 *Reconstitution and purification of Prom1 EVs*
85 To understand how Prom1 interacts with and reshapes native membranes, we sought a method to purify
86 Prom1 without disturbing protein-lipid interactions. Because Prom1 induces EV formation in epithelial
87 stem cells[22], we asked whether Prom1 can also form EVs in cultured cells. C-terminally Strep-tagged Prom1
88 was detected in immunoblots of the conditioned media from transfected cells, but not in cells treated
89 with a no-plasmid mock transfection (Fig 1A, 1B). To validate that the ~120 kDa Strep-reactive band we
90 observe is indeed Prom1-Strep, we immunoblotted with the Prom1-specific antibody AC133-1[37] and
91 observed robust staining (Fig 1C). To confirm that EV production is not an artifact of transfection, we
92 introduced Prom1-Strep into Expi293 cells by lentiviral transduction to generate a stable polyclonal
93 overexpression cell line. A Strep-reactive band consistent with mature Prom1 was detectable in the
94 conditioned media from these cells over several rounds of cell passaging (Fig S1A). We assessed the
95 protein composition of Prom1 EVs using SDS-PAGE and silver nitrate staining. Prom1 was a constituent of

96 our samples alongside several other proteins (Fig S1B). We cannot conclude whether these proteins
97 specifically interact with Prom1 in EVs, are hitchhikers enclosed within the EVs, or originate from
98 endogenous co-purifying EVs.
99
100 We next purified the Prom1 EVs using differential centrifugation, ultracentrifugal concentration, and size-
101 exclusion chromatography (SEC) based on isolation methods previously described for endogenous small
102 Prom1 EVs (Fig 1A)[22,38]. It is important to note that our purification protocol removes any large EVs and
103 midbody remnants, focusing our downstream experiments on small Prom1 EVs. Using dynamic light
104 scattering (DLS), we measured the solution sizes of the purified Prom1 EVs. The sample was monodisperse
105 with an average diameter of 164 ± 14 nm, considerably larger than previously reported 50-80 nm EVs
106 measured by negative-stain transmission electron microscopy (NS-TEM) in samples purified from
107 biological fluids[22] (Fig S1C). Upon treatment with PNGase F, an enzyme that cleaves *N*-glycan groups from
108 proteins, the ~120 kDa Prom1 gel band shifted down to its predicted molecular weight of 102 kDa (Fig
109 1D).
110
111 To verify that the purified particles are truly EVs (secreted particles with intact bilayer membranes), we
112 vitrified purified samples and imaged them using transmission cryo-electron microscopy (cryo-TEM) (Fig
113 1E). We observed spherical EVs with bilayer membranes (Fig 1E, inset). The diameters of EVs measured
114 from cryo-TEM images were bimodal with an average diameter of 117 ± 58 nm, somewhat lower than our
115 measurements from DLS (Fig 1G). We next used NS-TEM to directly compare our reconstituted Prom1 EVs
116 with previously characterized endogenous Prom1 EVs[22] (Fig 1F). We observed a distribution of largely
117 circular EVs ranging in size from ~50 nm to ~250 nm in diameter, but more skewed toward smaller
118 diameters than observed in the cryo-TEM data (Fig 1G). In addition, EVs had rough edges and internal
119 depressions in NS-TEM, a characteristic feature of EV fixation and dehydration[22] (Fig 1G). Because solution
120 DLS measurements (164 ± 14 nm) suggest slightly larger EV diameters than our NS-TEM (123 ± 73 nm) or
121 cryo-TEM (117 ± 58 nm) measurements, we speculate that sample fixation/dehydration or vitrification
122 may induce deformation and potentially fission of the reconstituted EVs. This effect may have similarly
123 impacted previous characterization of endogenous Prom1 EVs[22]. We conclude that reconstituted Prom1
124 EVs have similar morphology to endogenous EVs but may be slightly larger in size.
125
126 We next asked whether Prom1 in purified EVs retains known functional behavior of Prom1 from
127 endogenous membranes. Prom1 stably binds the retinal cadherin Pcdh21 in photoreceptors[12–14]. To

128 determine if Prom1 can co-traffic with Pcdh21 in our EV samples, we co-transfected Expi293 cells with
129 Strep-tagged Prom1 and Flag-tagged Pcdh21 and looked for the presence of each component in cells,
130 conditioned media (CM), and clarified conditioned media (CCM). Pcdh21 was only observed in CCM
131 samples when co-expressed with Prom1, indicating that Prom1 is necessary to traffic Pcdh21 into this
132 class of EVs (Fig 1H). To establish a direct interaction between Prom1 and Pcdh21, we co-expressed
133 Prom1-Strep with mNeonGreen-tagged Pcdh21 and immunopurified Prom1 from EVs solubilized with 1%
134 n-dodecyl-ß-D-maltoside (DDM). Pcdh21-associated mNeonGreen reproducibly co-purified with
135 detergent-solubilized Prom1 compared to a control condition lacking Prom1, indicating that the two
136 proteins physically interact in purified EVs (Fig 1I).
137

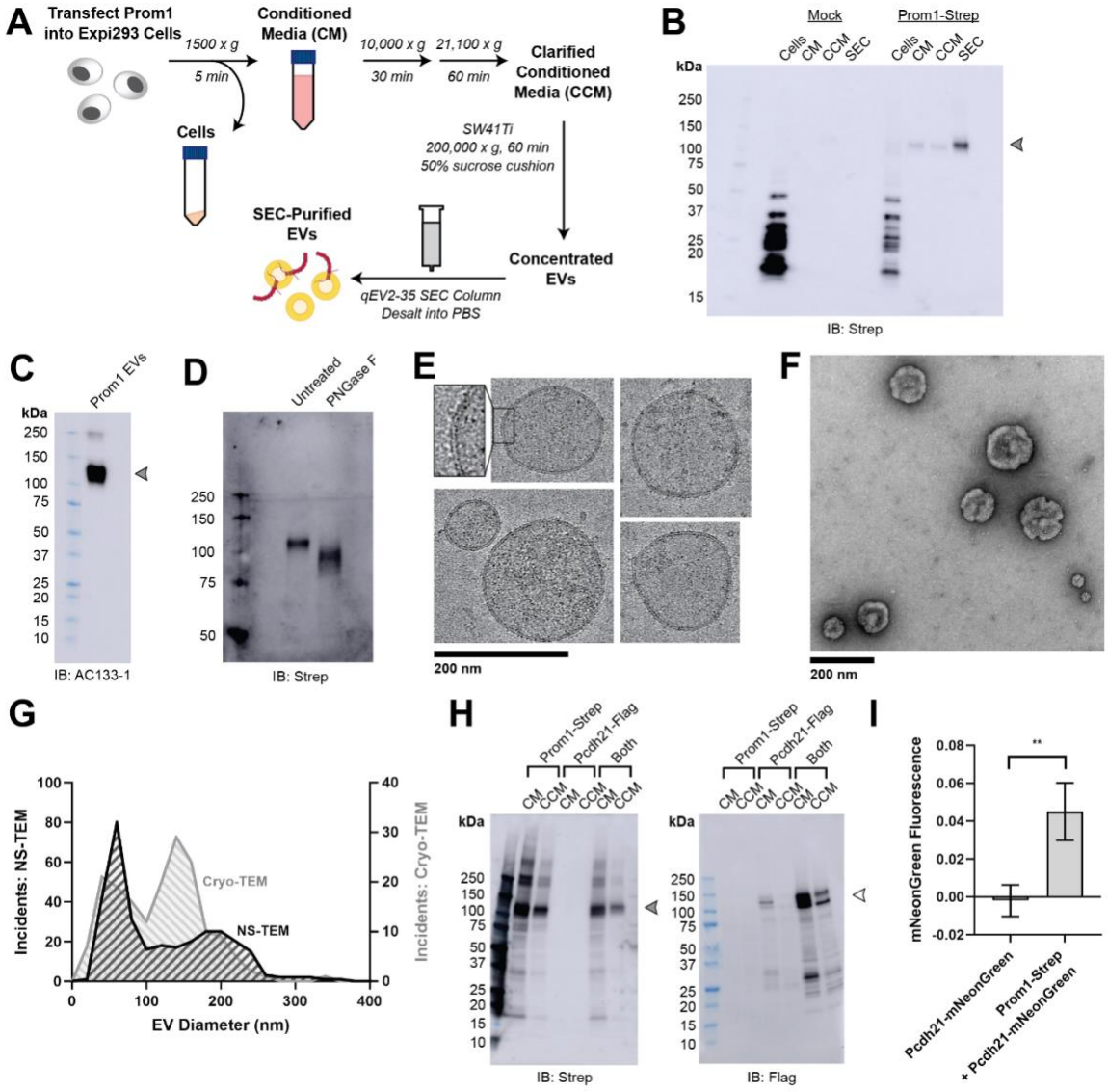

138

139 **Figure 1. (A)** EV expression and purification graphic protocol. **(B)** Anti-Strep immunoblot of cell pellet,
140 conditioned media (CM), clarified conditioned media (CCM), or SEC-purified EVs from mock-transfected
141 or Prom1-Strep-transfected Expi293 cells. Arrowhead indicates the expected molecular weight of
142 Prom1. **(C)** AC133-1 immunoblot of SEC-purified Prom1 EVs. Arrowhead indicates the expected
143 molecular weight of Prom1. **(D)** Anti-Strep immunoblot of Prom1 EVs treated with or without PNGase F
144 to remove *N*-glycan moieties. **(E)** Cryo-TEM images of purified Prom1 EVs. Inset image is magnified to
145 emphasize membrane bilayer density. Images are lowpass filtered to 5 Å to enhance contrast. **(F)** NS-
146 TEM image of purified Prom1 EVs. **(G)** Measured diameters of Prom1 EVs from Cryo-TEM or NS-TEM
147 images. (n = 322 and n = 176 for NS-TEM and cryo-TEM measurements, respectively.) **(H)** Anti-Strep
148 (Prom1) and anti-Flag (Pcdh21) immunoblots of CM and CCM from cells transfected with Prom1-Strep,
149 Pcdh21-Flag, or both. Note that Pcdh21 is only detected in CCM when co-expressed with Prom1. Filled
150 and empty arrows indicate expected molecular weights of glycosylated Prom1-Strep and Pcdh21-Flag,
151 respectively. **(I)** Comparative fluorescence measurements of Pcdh21-mNeonGreen co-
152 immunoprecipitated with or without Prom1-Strep (n = 3, ** $p < 0.01$ by Student's two-tailed unpaired t
153 test).

154

155 *Mutations in the Prom1 transmembrane domain impair EV formation*

156 Prom1 binds cholesterol in native membranes and the Prom1-cholesterol interaction is necessary for
157 remodeling the plasma membrane[21], but the mechanism of cholesterol-dependent Prom1 function is
158 unclear. We analyzed the sequence of human Prom1 to identify candidate cholesterol recognition amino
159 acid consensus (CRAC, [L/V]-$X_{1–5}$-[Y/F]-$X_{1–5}$-[K/R]) or mirrored CRAC (CARC, [K/R]-$X_{1–5}$-[Y/F]-$X_{1–5}$-[L/V])
160 sequences in the transmembrane helices, as these motifs often predict cholesterol binding in membrane
161 proteins[39]. Human Prom1 contained four CRAC and two CARC motifs, of which none were completely
162 conserved among metazoans and only one (CRAC-3) was modestly evolutionarily conserved (Figs S2A,
163 S2B). We therefore turned to a more comprehensive evolutionary analysis of prominin proteins to identify
164 evolutionarily conserved Prom1 transmembrane residues.

165

166 We curated prominin sequences from across eukaryotes, considering a prominin to be a sequence with
167 five predicted transmembrane helices, two large extracellular loops, two small intracellular loops, and
168 homology to annotated metazoan prominin sequences. Putative prominin sequences were identified
169 across metazoans as well as in fungi, excavates, SAR (stramenopiles, alveolates, and rhizarians), and green
170 plants (Figs S3A, S3B). Strikingly, Trp-795 was nearly perfectly conserved across metazoa and eukaryotic
171 outgroups, making it by far the most conserved residue (excluding Cys residues positioned to form
172 disulfides in AlphaFold2 models) across the curated prominin sequences (Figs 2A, S3A). The conserved

173 Trp-795 residue was of particular interest as a missense mutation at this site (W795R) is implicated in
174 hereditary CRRD cases[40].
175
176 We generated Prom1-Strep variants with mutations to disrupt each CRAC or CARC motif, the disease-
177 associated W795R mutation, and point mutations directed against residues predicted to be in close
178 contact with Trp-795 in Alphafold2 models (Fig 2B, Table ST1)[41]. We then assessed EV formation by
179 quantifying the Prom1-Strep signal secreted in EVs or retained in the cellular membranes. We found that
180 the W795R mutation to the Prom1 TM domain significantly disrupted the proportion of Prom1 secreted
181 in EVs (Figs 2C, S4 for raw blot images). This effect arose from both decreased expression of Prom1 and
182 increased retention of protein in cells, though neither of these measurements alone met our stringent
183 significance criteria. To better characterize the morphology of the Prom1 variants, we expressed and
184 purified a subset of mutant Prom1 EVs at larger scale. Each of the mutants produced EVs that are 150-200
185 nm in diameter and monodisperse by DLS analysis, with no mutant EV sizes deviating significantly from
186 that of WT Prom1 EVs (Fig 2D). Thus, transmembrane domain mutations in Prom1 primarily alter the
187 quantity of EVs produced rather than EV size.
188
189 To better understand the mechanism of reduced Prom1 EV formation by the CRRD-associated W795R
190 mutant, we engineered HeLa cells that stably express C-terminally StayGold-tagged WT (Prom1-SG) or
191 W795R Prom1 (Prom1[W795R]-SG) under the EF-1α promoter. Prom1-SG signal colocalized with Wheat
192 Germ Agglutinin (WGA)-stained plasma membrane, but Prom1[W795R]-SG was not present at the plasma
193 membrane and instead concentrated on WGA-positive intracellular features (Fig 2E). Despite the apparent
194 low signal of plasma-membrane localized Prom1-SG, line scan analysis shows correlation between Prom1-
195 SG signal across the cell junctions (Fig S5 left). In contrast, there is a marked absence of Prom1[W795R]-
196 SG signal localized on the plasma membrane (Fig S5 right). We infer that mStayGold-tagged W795R Prom1
197 is trafficked to the plasma membrane less efficiently than the mStayGold-tagged wild-type protein.
198

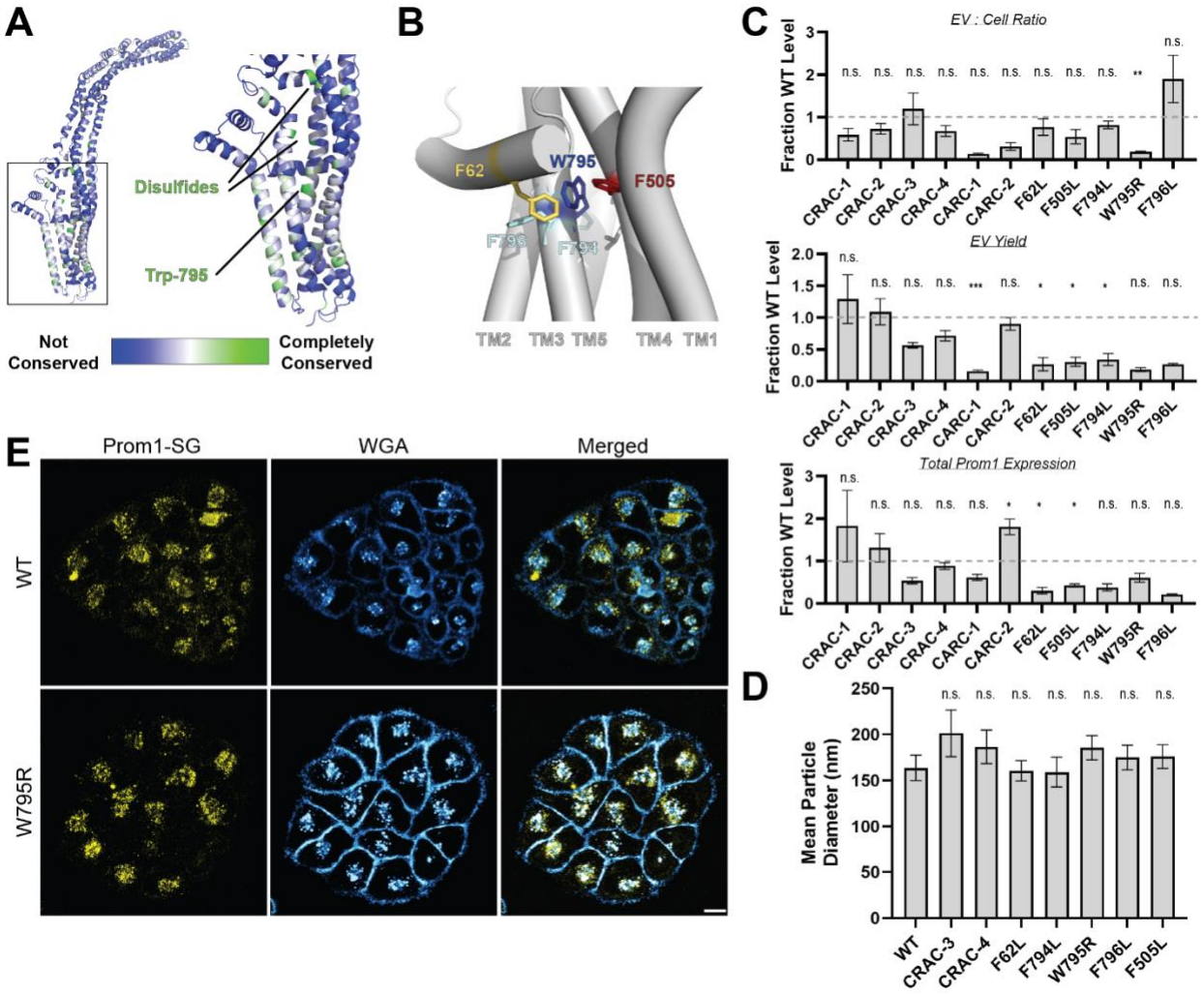

Figure 2. (A) AlphaFold2 model of human Prom1[41] with residues color-coded by level of conservation across a multiple-sequence alignment of metazoan prominin sequences. **(B)** Possible network of interactions between Trp-795 and several adjacent aromatic residues in human Prom1. **(C)** Quantification of anti-Strep immunoblots of cellular and clarified conditioned media pools of Prom1-Strep mutants relative to wild-type Prom1-Strep (n = 3, $^{n.s.}$ $p > 0.0045$, * $p < 0.0045$, ** $p < 0.0009$, *** $p < 0.00009$ by Student's two-tailed unpaired t test with significance thresholds adjusted by Bonferroni correction). Raw blot images from which measurements are derived are included in Supplemental Figure S4. **(D)** Mean particle diameter of purified Prom1-Strep EVs measured by dynamic light scattering. Error bars indicate S.D. (n = 5, $^{n.s.}$ $p > 0.007$, * $p < 0.007$ by Student's two-tailed unpaired t test with significance thresholds adjusted by Bonferroni correction). **(E)** Confocal fluorescence microscopy images of HeLa cells stably expressing WT (top) or W795R (bottom) Prom1-StayGold (yellow), stained with wheat germ agglutinin (WGA) (blue). Scale bar is 10 µm. Line scan traces across cell junctions are included in Supplemental Figure S5.

Prominin homolog Ttyh1 produces EVs

215 Tweety homology (Ttyh) proteins are proposed prominin homologs that share the five-transmembrane
216 topology of prominins but have shorter extracellular domains (~120 amino acids in Ttyh vs ~280 amino
217 acids in Prom)[20] (Fig 3A). Prominin and Ttyh both traffic to the plasma membrane and associate with
218 protrusive membrane structures[20,21,27,34–36]. Given the predicted sequence homology between Prom and
219 Ttyh, we hypothesized that Ttyh may also produce EVs. Evolutionary analysis of metazoan Ttyh proteins
220 does not indicate conserved CRAC or CARC sites, nor does it suggest any conserved transmembrane
221 residue analogous to Trp-795 in metazoan prominins (Fig 3B).
222
223 We expressed C-terminally Strep-tagged Ttyh1 in Expi293 cells and purified EVs using the same procedure
224 as for Prom1 EVs (Fig 1A). We detected Ttyh1-Strep in CM, CCM, and SEC-purified EV fractions (Fig 3C).
225 Dynamic light scattering indicated that purified Ttyh1 EVs are monodisperse with an average diameter of
226 180 ± 10 nm, similar to the average diameter of WT Prom1 EVs (164 ± 14 nm) (Fig S6A).
227
228 We next characterized the morphology of purified Ttyh1 EVs using NS-TEM. We found that Ttyh EVs
229 adopted striking long and bent tubular structures with much higher frequency than Prom1 EVs (6.4% of
230 Ttyh1 EVs versus 0.3% of Prom1 EVs, n = 1357 and n = 322 respectively) (Figs 3D, 3G). Ttyh1 EVs visualized
231 by NS-TEM were on average smaller than Prom1 EVs (Figs 3F, 3G), and were similarly smaller than
232 expected from solution DLS measurement (Fig. S1C). Furthermore, we observed that the smallest Ttyh1
233 EVs were similar in diameter to the short-axis caliper diameter of the tubular EVs (42 ± 6 nm) and we
234 observed cases where tubular EVs appeared to be in the process of dividing into smaller EVs (Figs 3D white
235 arrowheads, 3F). Although the NS-TEM conditions deviate from a solvated physiological state, they do
236 suggest that Ttyh1 supports comparatively greater membrane curvature than Prom1 in these EVs.
237
238 We further analyzed Ttyh1 EVs by cryo-TEM to verify that the purified sample indeed contained EVs with
239 intact bilayer membranes (Fig 3E). Like Prom1 EVs, Ttyh1 EVs have a bimodal size distribution with local
240 maxima around 60 nm and 140 nm (Fig 3F). We also observed a population of EVs exhibiting the tubular
241 phenotype seen in NS-TEM that again substantially exceeded that seen with Prom1 EVs (8.8% of Ttyh1
242 EVs versus 0.8% of Prom1 EVs, n = 2224 and n = 176 respectively) (Fig 3G). This supports the observation
243 that EV bending is more frequent in Ttyh1 EVs than Prom1 EVs.
244
245 Molecular crowding is known to contribute to membrane bending[42]. To test if Ttyh1 may promote EV
246 membrane bending through a crowding mechanism, we quantified relative protein-to-membrane ratios

247 for Prom1 and Ttyh1 EVs. From identical amounts of transfected cell media, purified EVs contained 8.8 ±
248 1.0-fold more Ttyh1 protein than Prom1 (Figs 3H, S6B). Both Prom1 and Ttyh1 EV membrane surface area
249 was significantly more abundant than the background level of EVs produced in a mock-transfected control
250 culture, but Ttyh1 produced 5.6 ± 0.8-fold more total EV membrane than Prom1 (Figs 3I, S6C). From these
251 measurements, we estimate that Ttyh1 is present at ~5-fold higher concentration in EV membranes (Fig
252 S6D). Thus, molecular crowding effects may be a factor contributing to the increased membrane bending
253 we observe in Ttyh1 EVs.
254
255 To further characterize purified Prom1 and Ttyh1 EVs, we subjected purified EVs to equilibrium sucrose
256 gradient sedimentation to resolve populations by density. We observed a single population of Prom1 EVs
257 (centered on fraction 7) but resolved two distinct populations of Ttyh1 EVs with densities lower (centered
258 on fraction 6) and higher (centered on fraction 9) than the Prom1 EVs (Fig 3J). When Prom1 and Ttyh1
259 were co-expressed, we observed that the resulting EVs contained more Prom1 than Ttyh1 but followed
260 the bimodal distribution of Ttyh1 EVs (Fig 3K). Immunoblots of the sucrose gradient fractions showed that
261 co-expressed Prom1 and Ttyh1 peak in the same sucrose gradient fractions, suggesting that Prom1 and
262 Ttyh1 co-elute in the same EV populations (Fig 3K, 3L).
263

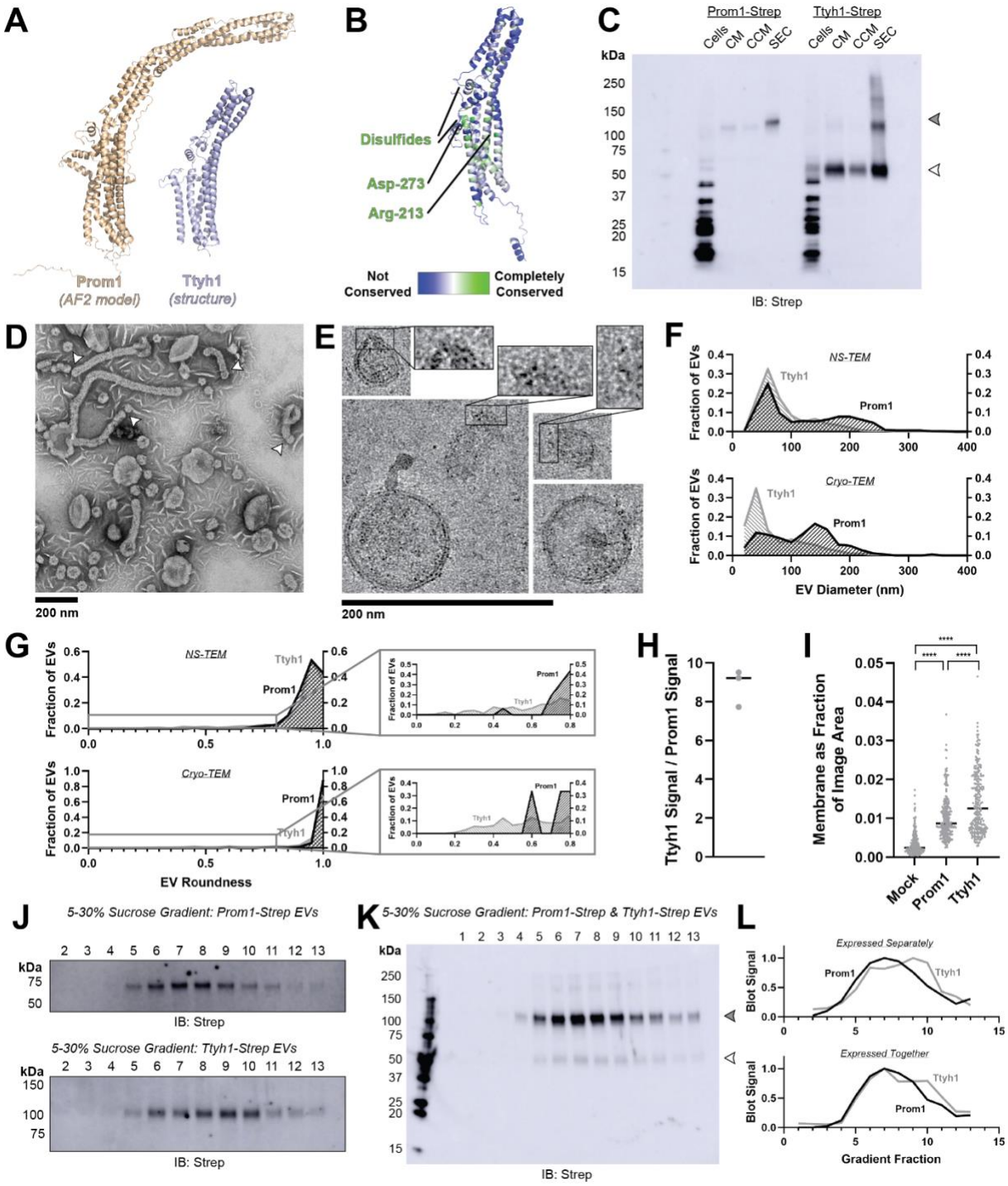

Figure 3. (A) Comparison of a Ttyh1 subunit from cryo-TEM structure 7P5J[32] with an AlphaFold2-predicted Prom1 monomer[41]. **(B)** Residue-level conservation among metazoan Ttyh proteins plotted onto a subunit of human Ttyh1. No residue analogous to Prom1 Trp-795 is present in Ttyh. **(C)** Anti-strep immunoblot comparing Prom1-Strep EVs and Ttyh1-Strep EVs throughout different stages of purification. Filled and empty arrowheads indicate the expected positions of Prom1 and Ttyh1, respectively. Doublet and higher bands in Ttyh1 lanes are products of on-gel disulfide crosslinking in

concentrated samples. **(D)** Representative NS-TEM images of Ttyh1-Strep EVs. White arrowheads indicate possible sites of EV fission. **(E)** Representative cryo-TEM images of Ttyh1-Strep EVs. Magnified insets show bilayer density at highly curved membrane segments. Images are lowpass filtered to 5 Å to enhance contrast. **(F)** Comparison of Prom1 or Ttyh1 EV diameter in NS-TEM or cryo-TEM images. (n = 322, n = 1357, n = 176, and n = 2224 for Prom1 NS-TEM, Ttyh1 NS-TEM, Prom1 cryo-TEM, and Ttyh1 cryo-TEM measurements, respectively.) **(G)** Comparison of Prom1 or Ttyh1 EV roundness in NS-TEM or cryo-TEM images. Secondary plots only include EVs with roundness ≤ 0.8. (n = 322, n = 1357, n = 122, and n = 1546 for Prom1 NS-TEM, Ttyh1 NS-TEM, Prom1 cryo-TEM, and Ttyh1 cryo-TEM measurements, respectively.) **(H)** Quantification of Prom1 and Ttyh1 protein levels in EVs from anti-Strep Western blots (n = 3). Immunoblots used for quantification are included in Supplementary Figure S6A. **(I)** Quantification of total EV membrane area from NS-TEM micrographs (n = 236, *** $p < 0.001$ by unpaired Mann-Whitney test). Representative micrographs used for quantification are included in Supplementary Figure S6B. **(J)** Anti-strep immunoblots of fractions from sucrose gradient equilibrium sedimentation of Prom1-Strep EVs (top) or Ttyh1-Strep EVs (bottom). **(K)** Anti-strep immunoblots of fractions from sucrose gradient equilibrium sedimentation of EVs from cells co-expressing Prom1-Strep and Ttyh1-Strep. Filled and empty arrowheads indicate the expected positions of Prom1 and Ttyh1, respectively. **(L)** Quantification of immunoblots in panels *K* (top) and *L* (bottom).

Ttyh1 binds cholesterol less stably than Prom1

Because cholesterol interaction is known to regulate membrane bending by Prom1, we asked whether Prom1 and Ttyh1 bind cholesterol similarly[20,21]. To comparatively measure binding, we developed a cholesterol co-immunopurification assay (hereafter referred to as chol-IP) to quantify interaction of Prom1 with fluorophore-labeled cholesterol (Fig 4A). Prom1-Strep or Ttyh1-Strep were transfected into Expi293 cells, and cells were labeled with a low concentration of fluorescent cholesterol. EVs were purified from the conditioned media, solubilized with nonionic detergent (1% DDM), and immunoprecipitated with Strep resin trace labeled with blue fluorescent protein (mTagBFP2-Strep). We then collected epifluorescence micrographs of the resin particles, computationally segmented and filtered each image, and quantified bound cholesterol using mTagBFP2 as a normalizing control (Fig 4A). This approach permits sensitive quantification of bound lipid while efficiently excluding autofluorescent and refractive artifacts.

We performed chol-IP analysis on Prom1 or Ttyh1 EVs labeled with BODIPY-cholesterol. Surprisingly, fluorescent cholesterol robustly copurified with Prom1 but not with Ttyh1 (Fig. 4B). To verify that this difference is not a result of nonspecific fluorophore-protein interactions, we replicated the observation using a different fluorescent cholesterol analog (AlexaFluor647-cholesterol) (Fig S7). We further verified that the cholesterol is specifically bound to Prom1 by quantifying bound cholesterol at different concentrations of solubilizing detergent (Fig 4C). Nonspecifically associated fluorescent cholesterol in

307 Ttyh1 samples is delipidated at 0.04-0.2% DDM, 5-25-fold below the assay working concentration,
308 suggesting that the assay informs on specific lipid binding that is resistant to delipidation. Although this
309 method cannot inform on transient or kinetically unstable protein-lipid interactions, we infer that Prom1
310 and Ttyh1 differ in how stably they interact with membrane cholesterol.
311
312 Given the striking difference in cholesterol binding stability between Prom1 and Ttyh1, we next asked
313 whether Prom1 mutants also disrupt cholesterol interaction stability. We purified BODIPY-cholesterol-
314 labeled EVs produced by WT and mutant forms of Prom1 and subjected equal input concentrations of
315 Prom1 to chol-IP analysis. To our surprise, none of the mutants substantially disrupted cholesterol
316 binding, but the W795R mutant and the CARC-1 mutants bound cholesterol significantly more stably than
317 WT Prom1 (Fig 4D). We chose to focus our efforts on the W795R mutant as it is a naturally occurring
318 single-residue mutation with exceptional evolutionary conservation and a clinically validated disease
319 phenotype. To verify that differences in cholesterol binding between wild-type and W795R Prom1 do not
320 arise from a gross oligomerization defect, we purified EVs from cells co-transfected with Strep-tagged and
321 mScarlet-tagged Prom1 and measured co-purification of Prom1-mScarlet on Strep resin. Prom1 W795R
322 co-purified with ~60% as much mScarlet fluorescence as WT Prom1, indicating that W795R indeed
323 multimerizes, albeit with reduced efficiency (Fig 4E). Comparative analysis of EV Yield (Fig. 2C) and
324 cholesterol bound (Fig. 4D) indicates that though there may be a weak inverse correlation between
325 cholesterol binding and stable cholesterol binding, W795R, CARC-1, and CARC-2 are outliers that bind
326 cholesterol exceptionally tightly (Fig. 4F).
327

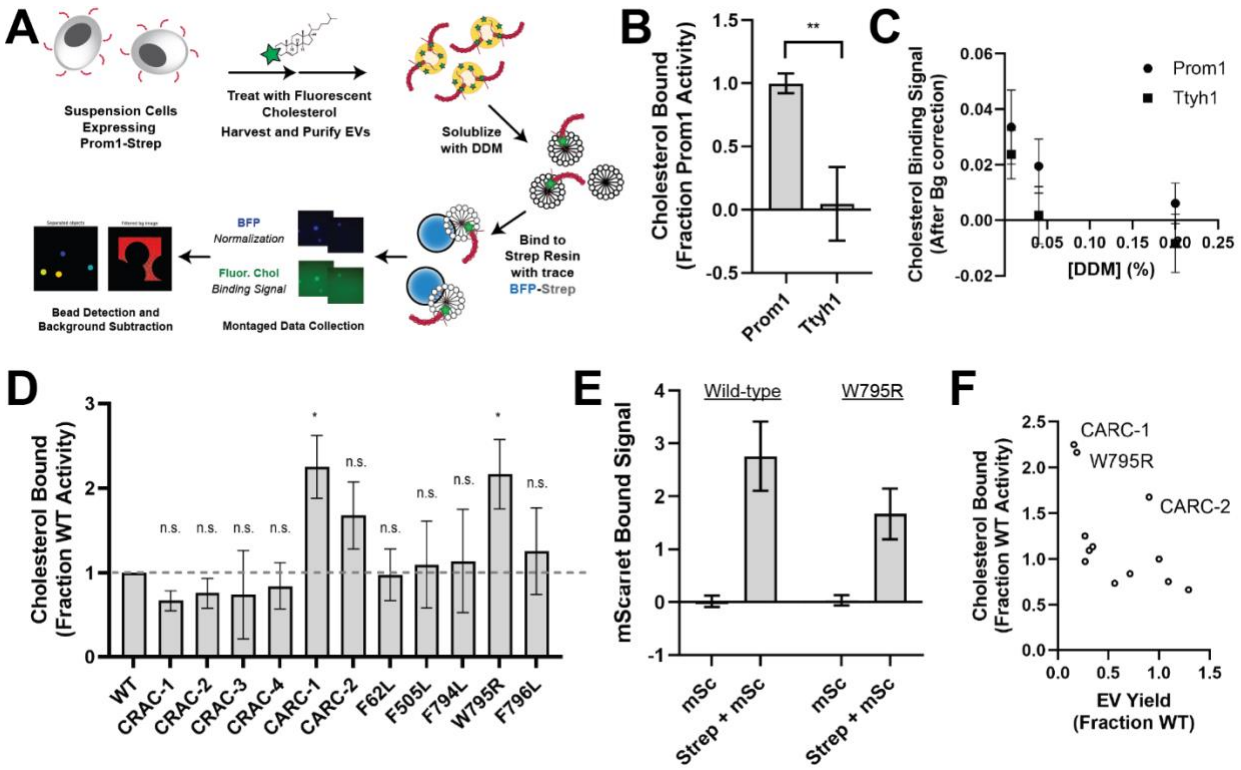

Figure 4. (A) Cholesterol co-immunoprecipitation (Chol-IP) assay graphic protocol. **(B)** Comparison of relative cholesterol bound by Prom1-Strep or Ttyh1-Strep (n = 3, ** $p < 0.01$ by Student's two-tailed unpaired t test). **(C)** Fluorescent cholesterol co-immunopurified by Prom1-Strep or Ttyh1-Strep at different concentrations of DDM detergent. Error bars indicate S.D. (n = 3). **(D)** BODIPY-cholesterol binding measurements for WT and mutant variants of Prom1. Error bars indicate S.D. (n = 3, n.s. $p > 0.0045$, * $p < 0.0045$ by Student's two-tailed unpaired t test with significance thresholds adjusted by Bonferroni correction). **(E)** Red fluorescence signal from anti-Strep immunopurification of DDM-solubilized EVs from cells expressing Prom1-mScarlet ("mSc") or both Prom1-mScarlet and Prom1-Strep ("Strep + mSc"). Error bars indicate S.D. (n = 3). **(F)** Comparison between EV yield (Fig. 2C) and chol-IP fluorescent cholesterol binding (Fig. 4D), with notable outliers labeled.

Cholesterol binding stability inversely correlates with Prom1 EV membrane bending

Because Ttyh1 promotes greater membrane curvature than Prom1 but does not stably bind cholesterol, we hypothesized that cholesterol binding stability may contribute to negative regulation of membrane bending by prominin-family proteins. If this is the case, then W795R Prom1, which binds cholesterol more stably than WT protein, should not produce EVs that exhibit the tubular morphology observed in Ttyh1 EVs. After purifying W795R Prom1 EVs, we observed a similar solution size for WT (164 ± 14 nm) and W795R EVs (186 ± 13 nm) (Fig S8). We measured the size and shape of W795R EVs by cryo-TEM and observed largely spherical vesicles with some local deformations, similar to what we observed with WT

348 Prom1 EVs (Fig 5A). Generally, WT and W795R Prom1 EVs are both spherical, with W795R having no
349 vesicles that fall into our tubular morphology classification (n = 1211) (Fig 5B). Though both large and
350 small diameter EV populations were observed by cryo-TEM, W795R Prom1 had a larger fraction of small
351 EVs than WT Prom1, indicating possible decreased stability or increased fissile propensity in the W795R
352 Prom1 EVs (Fig 5C).
353
354 If stable cholesterol binding negatively regulates membrane bending, then depleting cholesterol away
355 from EV membranes could induce a Ttyh1-like morphology in Prom1 EVs. We tested this model directly
356 by purifying WT Prom1 or Ttyh1 EVs and treating them with methyl beta cyclodextrin (mBCD), a
357 compound that extracts cholesterol from membranes[21,43]. After re-purifying EV samples away from free
358 mBCD and mBCD-cholesterol complexes, Prom1 EVs treated with mBCD (2.5-10 mM) exhibited a decrease
359 in cholesterol content (Fig 5D). A control set of Ttyh1 EVs treated with 0 or 10 mM mBCD showed a similar
360 change in cholesterol content (Fig 5D). Treated and untreated EVs were then analyzed by NS-TEM to
361 compare EV size and morphology (Fig 5E). We observed a 5.4-fold increase in the fraction of Prom1 EVs
362 that deviated from spherical membrane topology after 10 mM mBCD treatment compared to untreated
363 EVs (3.0% versus 0.6% of EVs, n = 232 and n = 356 respectively) (Fig 5F). Importantly, identical treatment
364 of Ttyh1 EVs was used as a nonspecific control for cholesterol depletion from EVs. Ttyh1 EVs treated with
365 mBCD under identical conditions only showed a 1.4-fold increase in deformed EVs (2.1% at 10 mM mBCD
366 versus 1.5% in mock-treated EVs, n = 433 and n = 535 respectively) (Fig 5F). Thus, cholesterol-depleted
367 Prom1 EVs are more prone to membrane deformation than untreated EVs.
368

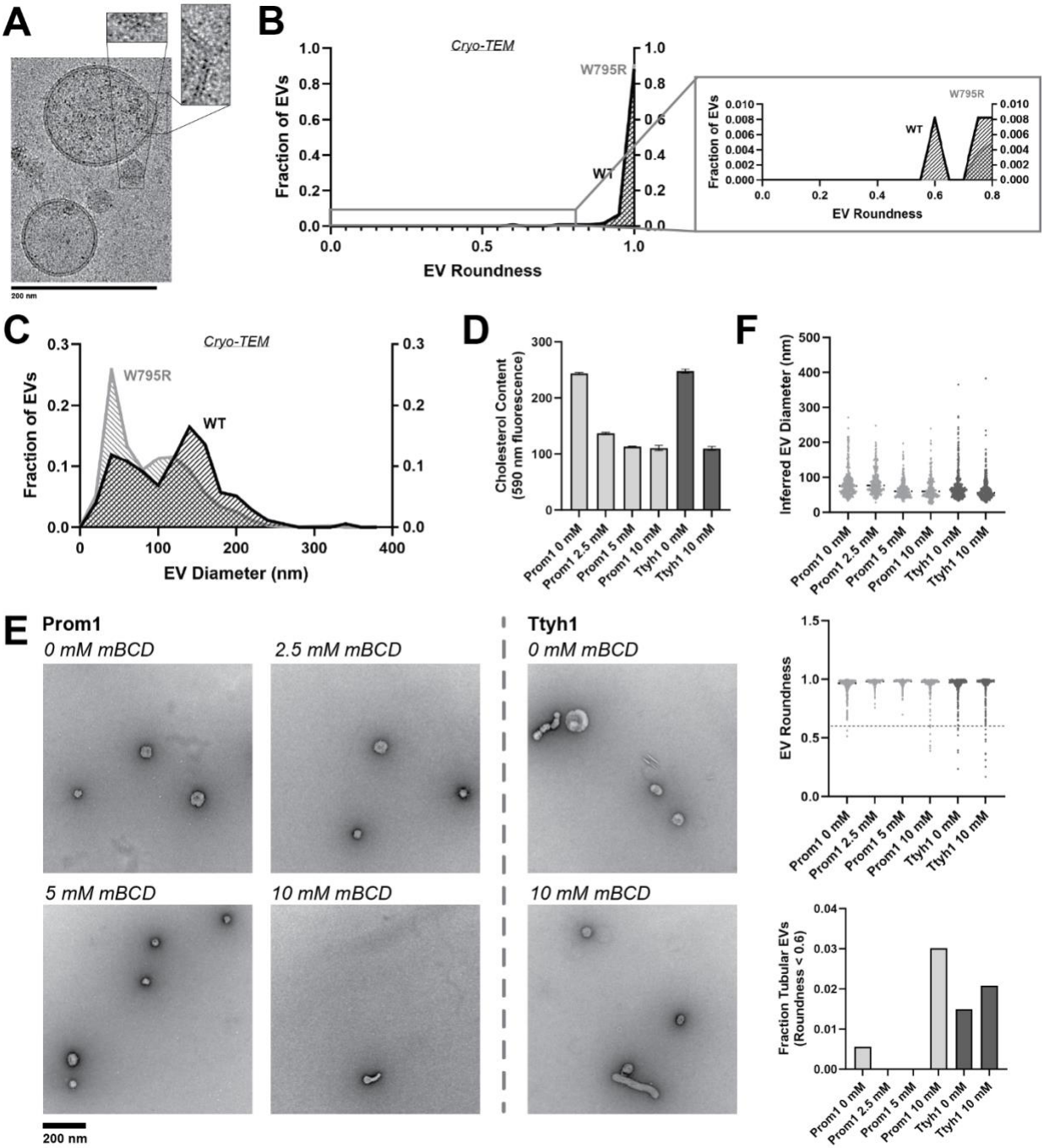

Figure 5. (A) Representative cryo-TEM images of W795R Prom1-Strep EVs. Magnified insets show bilayer density. Images are lowpass filtered to 5 Å to enhance contrast. **(B)** Comparison of WT or W795R EV roundness in cryo-TEM images. Secondary plot only includes EVs with roundness ≤ 0.8. (n= 176 and n = 1211 for WT and W795R Prom1 cryo-TEM measurements, respectively.) **(C)** Comparison of WT or W795R Prom1 EV diameter in cryo-TEM images. (n= 122 and n = 821 for WT and W795R Prom1 cryo-TEM measurements, respectively.) **(D)** Cholesterol content of Prom1 or Ttyh1 purified EV samples after treatment with methyl-beta cyclodextrin (mBCD). Error bars indicate S.D. (n = 3). **(E)** Representative NS-

377 TEM images of purified mBCD-treated EVs. **(F)** Quantification of EV diameter (*top*) and roundness
378 (*middle*) from NS-TEM images, as well as quantification of tubulated EVs (roundness < 0.6) (*bottom*).

379

380

381 **Discussion**

382 *Prom1 and Ttyh1 bend membranes and form EVs*

383 We report here that both Prom1 and Ttyh1 can induce EV formation in cultured cells upon overexpression
384 (Figs 1B, 3C). Though we have not examined whether Ttyh1 endogenously induces EV formation, we note
385 that it is sufficient to do so in a recombinant system with similar or higher efficiency than Prom1. Given
386 similar membrane remodeling behavior of Prom1 and Ttyh1 in cell culture[20,35], Ttyh1 EVs may form by a
387 similar mechanism to Prom1 EV formation. We find that Prom1 and Ttyh1 form EVs that are of similar size
388 and that the two proteins exist in the same pool of EVs when co-expressed (Figs 3K, 3L).

389

390 Membrane bending by Prom1 is critical for maintaining outer segment membrane homeostasis in
391 photoreceptors. Intriguingly, photoreceptors with impaired expression of the disc rim stabilizing protein
392 Peripherin accumulate EVs 200-280 nm in diameter at the outer segment base[44]. We observe formation
393 of Prom1 EVs of relatively similar size in our reconstituted system (Fig S1C). This may be an example of
394 endogenous regulation of Prom1-induced membrane curvature, with curvature-stabilizing proteins like
395 Peripherin preventing the evaginating membrane from budding into EVs.

396

397 *Ttyh1 forms EVs with membranes that are more tubulated than Prom1 EV membranes*

398 Ttyh1 produces EVs similar in size and density to Prom1 EVs (Figs S6A, 3J, 3K, 3L). However, Ttyh1 EVs are
399 dramatically more tubulated that Prom1 EVs (Figs 1E, 1F, 3D, 3E, 3G). Several factors could contribute to
400 this increase in membrane bending. First, Ttyh1 is present in EVs at concentrations approximately 5-fold
401 higher than Prom1 (Figs 3H, 3I). Membrane proteins can induce curvature through molecular crowding
402 when enriched at sufficiently high local concentrations[42]. Second, Ttyh1 co-purifies with cholesterol less
403 efficiently than Prom1 does (Fig 4B). A confounding effect in our experiments is that molecular crowding
404 may also alter the efficiency with which cholesterol is extracted from EV membranes by detergent.
405 Although we did not observe a kinetically stable interaction between Ttyh1 and cholesterol, it remains to
406 be conclusively determined whether Ttyh1-cholesterol interactions occur in native membranes. Ideally,
407 molecular-crowding and cholesterol-binding effects could be differentiated by modulating protein-to-lipid
408 ratios in EV membranes. Unfortunately, our native purified EVs do not provide a tractable path to perform

409 these experiments. Future experiments reconstituting Prom1 and Ttyh1 into artificial liposomes with
410 variable cholesterol content will be necessary to fully elucidate the mechanistic differences in membrane
411 bending between Prominin and Ttyh proteins.
412
413 *Cholesterol binding stability may contribute to membrane bending regulation by Prom1*
414 We find here that Prom1 in EVs forms a stable interaction with cholesterol that is resistant to delipidation
415 by nonionic detergent (Figs 4B, 4C). A disease-associated mutation in a strikingly conserved residue in the
416 fifth transmembrane helix of Prom1, W795R, substantially stabilizes cholesterol binding (Figs 2A, 4D). In
417 AlphaFold2 models, Trp-795 forms a series of base-stacking interactions with Phe residues in neighboring
418 transmembrane helices (Fig 2B)[41]. We find that conservative mutations in several of these adjacent
419 aromatic residues impair EV formation by Prom1, but do not mimic the stable cholesterol binding of
420 W795R (Figs 2C, 4D, 4F). Cholesterol is asymmetrically distributed in eukaryotic membranes, with a bias
421 toward the outer leaflet[45]. Prom1 Trp-795 is predicted to be positioned toward the outer leaflet, possibly
422 potentiating interactions with cholesterol. We also observe increases in cholesterol binding stability for
423 mutations to two CARC domains in Prom1 (Fig 4D, 4F). This effect could arise because these residues
424 interface with cholesterol or because they destabilize the transmembrane domain in a manner that
425 mimics the effect of the W795R mutation. Given the poor evolutionary conservation of the two CARC
426 motifs in human Prom1, we favor the latter explanation.
427
428 We further show that the W795R mutation prevents efficient trafficking of mStayGold-tagged Prom1 to
429 the plasma membrane (Fig 2E). W795R Prom1 is expressed but primarily localizes to WGA^+ intracellular
430 vesicles. This observation explains the low yield of W795R EVs produced in cell culture (Fig 2C). Several
431 studies have demonstrated that protein trafficking through the endomembrane system is sensitive to
432 cholesterol levels[46,47], and our findings may suggest an as-yet undefined role for cholesterol in Prom1
433 membrane trafficking as well.
434
435 *Prominin and Tweety homology proteins are homologous proteins that both promote EV formation*
436 Prominin and Ttyh proteins are both biologically implicated in membrane bending. Prominins localize to
437 cholesterol-rich domains of the plasma membrane and drive protrusion-shed EV formation in
438 differentiating stem cells[21,22,24]. Ttyh proteins are associated with dendritic spikes in healthy neurons and
439 with tumor microtube formation in aggressive astrocytoma[27,34–36]. Given their sequence homology and
440 transmembrane topology, and their similarities in membrane localization, membrane bending and EV

441 formation behavior, we suggest that Prom and Ttyh proteins be considered members of a broader
442 prominin family of membrane remodeling proteins. Further work will be required to fully characterize the
443 functional specialization of Prom and Ttyh proteins.
444
445
446 **Materials and Methods**
447 *Expression Constructs*
448 All Prom1 expression constructs were generated by site-directed mutagenesis from pCS2-Prom1-YFP (a
449 gift from N. Sasai, Nara Institute of Science and Technology). The base Prom1 construct used is the human
450 S1 isoform (NCBI accession NP_001139319.1)[48]. Prom1-Strep was subcloned into pLV-EF1a vector (a gift
451 from K. Hochedlinger, Massachusetts General Hospital) for lentiviral transduction. Human Pcdh21 isoform
452 1 (NCBI accession NP_149091.1) was synthesized (GenScript) and cloned into a pCDNA3.1 vector (Thermo
453 Fisher) for mammalian cell transfection. mTagBFP2 was subcloned from pBAD (Addgene #54572, a gift
454 from Michael Davidson) into a pET28a vector with a C-terminal Strep tag for bacterial overexpression.
455 Ttyh1 was expressed from a pLX304 vector after addition of C-terminal Strep and His tags to an existing
456 construct (Addgene #161676, a gift from Mike McManus). To stably express fluorescently tagged Prom1
457 WT and W795R variants in HeLa cells for live cell imaging, Prom1-StayGold and Prom1[W795R]-StayGold
458 sequences were synthesized (GenScript) and cloned into a P2555 vector (a gift from S. Jakobs, Max Planck
459 Institute for Biophysical Chemistry) to yield constructs pAH18 and pAH20, respectively.
460
461 *Cell Line Construction*
462 Cell lines were regularly tested for mycoplasma contamination. Lentiviral transduction of Prom1-Strep
463 into Expi293 cells was performed using a modification of published protocols[49,50]. Briefly, lentiviral
464 particles were produced in 293T cells (ATCC) by transient transfection of pLV-EF1a-Prom1-Strep with
465 VSVG and Delta 8.9 plasmids (a gift from K. Hochedlinger, Massachusetts General Hospital) using the
466 Lipofectamine 3000 system (Thermo Fisher) and incubated overnight at 37 °C, 5% CO_2. Expi293 cells
467 (Thermo Fisher) raised for several passages in suspension culture were seeded onto adherent tissue
468 culture plates in adherent culture media (DMEM (Gibco) supplemented with 10% Fetal Bovine Serum
469 (Gibco) and 1x Penicillin/Streptomycin (Gibco)) and incubated overnight at 37 °C, 5% CO_2 to form an
470 adherent monolayer. Transfected cells were exchanged into fresh adherent culture media. Culture media
471 was harvested after an additional 48 h, filtered through a 0.45 µm vacuum unit, and concentrated from
472 70 mL to 0.3 mL in PBS buffer by ultracentrifugation according to established protocols[50]. Adherent

473 Expi293 cells were infected with concentrated lentiviral particles at 75% confluency in adherent culture
474 media supplemented with 8 µg/mL polybrene (Sigma-Aldrich), then incubated for 48 h at 37 °C, 5% CO_2.
475 Cells were gently washed with PBS, exchanged into adherent culture media, and incubated for 24 h at
476 37 °C, 5% CO_2. Subsequently, the cells were subjected to antibiotic selection by exchange into adherent
477 culture media containing 2 µg/mL blasticidin (Gibco) for 10 days with regular exchange into fresh selective
478 media and passaging to prevent cells from achieving full confluency. Selection was considered complete
479 when the majority of cells died and antibiotic-resistant foci recolonized the culture plate. The cells were
480 then trypsinized (Gibco) and transitioned back to suspension culture in modified suspension culture media
481 (Expi293 media (Gibco) supplemented with 1% Fetal Bovine Serum) at a density of 1.0 x 10^6 live cells per
482 mL of culture and incubated for 48 h at 37 °C, 8% CO_2 with 125 rpm rotation. Once the suspension culture
483 reached a density of 3.0 x 10^6 live cells per mL of culture, cells were re-passaged in 1.0 x 10^6 live cells per
484 mL of culture in fresh modified suspension culture media supplemented with 1.5 µg/mL Blasticidin, and
485 subsequently re-passaged into this media condition every 2 days.
486
487 Stable cell lines were constructed using lentiviral and AAV transduction methods according to established
488 protocols[49,50]. For generation of stable HeLa cells expressing WT Prom1-StayGold and Prom1[W795R]-
489 StayGold off the AAVS1 locus, the donor plasmids pAH18 or pAH20 were co-transfected with the nuclease
490 plasmid PX458-AAVS1 (a gift from S. Jakobs, Max Planck Institute for Biophysical Chemistry) using
491 Lipofectamine 3000 (Thermo Fisher). Transfected cells were selected with 10 µg/mL blasticidin (Gibco)
492 starting 48 h post-transfection for 7 days. Stable clones were expanded for 10 days, and single-cell GRP-
493 positive clones were obtained using a FACS AriaII Cell Sorter (BD Biosciences). After clonal expansion,
494 positive clones were detected and verified by fluorescence imaging.
495
496 *Prom1 and Ttyh1 EV Reconstitution*
497 Prom1 and Ttyh1 EVs were reconstituted by expression in Expi293 suspension cells. Briefly, Expi293 cells
498 grown in serum-free Expi293 media at 37 °C, 8% CO_2 with 125 rpm rotation to a density of 3.0 x 10^6 live
499 cells per mL of culture were transiently transfected with an appropriate plasmid at 1 µg of DNA per 1 mL
500 of culture using the Expifectamine transfection kit (Thermo Fisher) according to the manufacturer
501 protocol. After 48 h, cultures were centrifuged for 5 min at 500 x *g*, the media discarded, and the cells
502 resuspended in the same volume of fresh Expi293 media and returned to incubate for an additional 48 h.
503 After this final incubation, cultures were centrifuged for 5 min at 1500 x *g* and the conditioned media
504 transferred to clean 50 mL conical tubes.

505

506 EVs labeled with fluorescent cholesterol analogs were generated as described above with the following
507 modifications. Two days after transfection, cells were transferred to 50 mL conical tubes, centrifuged for
508 5 min at 500 x *g*, then resuspended in an equal volume of Expi293 media with fluorescent cholesterol
509 added to a final concentration of 4 µM. Cells were transferred back to shaker flasks and incubated for 24
510 h before conditioned media was harvested.

511

512 *EV Purification*

513 Conditioned media was clarified immediately after harvest by centrifuging for 30 min, 10,000 x *g* at 4 °C;
514 then transferring the supernatant to clean tubes and centrifuging again for 1 h, 21,100 x *g* at 4 °C. The
515 supernatant was transferred to clean 50 mL conical tubes and stored at 4 °C until ready for further
516 purification. Clarified conditioned media was transferred to Seton 7030 tubes and each tube underlaid
517 with a 100 µL cushion of 50% sucrose. Tubes were centrifuged in an SW-41 Ti rotor (Beckman Coulter) for
518 1 h, 36,000 rpm at 4 °C, then ≥ 200 µL of volume was harvested from the bottom of each tube. In cases
519 where the total harvested volume exceeded 500 µL, the harvested volume was diluted to 11 mL with
520 sterile-filtered PBS buffer, transferred to a final Seton 7030 tube, underlaid with a 100 µL cushion of 50%
521 sucrose, re-centrifuged as described above, and 500 µL of volume harvested from the bottom of the tube.
522 Concentrated EVs were then purified by size exclusion chromatography into sterile-filtered PBS buffer
523 using qEV2-35 nm gravity columns (Izon) at ambient temperature (0.5 mL load volume, 2.5 mL void
524 volume, 1.2 mL harvest volume). Purified EVs were stored at 4 °C for up to 8 weeks, over which time no
525 evidence of sample degradation was observed.

526

527 *Immunoblots*

528 Protein samples were run on 4-20% or 7.5% Mini-PROTEAN TGX SDS-PAGE gels (BioRad), then transferred
529 to PVDF membranes using the TurboBlot semi-dry transfer system (BioRad). Blots were washed briefly 3
530 times with 10 mL of PBST buffer, then incubated for 1-2 h at room temperature in PBST with blocking
531 agent (5 mg/mL Bovine Serum Albumin (Sigma Aldrich) for anti-Strep blots, 5% nonfat dry milk for all other
532 blots). Blocking solution was removed and primary antibody solution in PBST with blocking agent (1:2000
533 rabbit anti-Strep (Abcam #76949), 1:4000 mouse anti-Flag (Millipore Sigma #F3165), 1:2500 mouse
534 AC133-1 (Miltenyi #130-111-756)) for 2 h at ambient temperature or for 12-72 h at 4 °C. The blots were
535 then washed 3 times for 5-10 min with 10 mL PBST. Secondary antibody solution (1:5000 ECL anti-Mouse
536 (Cytiva) or 1:10,000 ECL anti-Rabbit (Cytiva)) in PBST with appropriate blocking agent was then added to

537 the blots and incubated for 1 h at ambient temperature. Blots were incubated with 5 mL Western Lighting
538 ECL solution (PerkinElmer) for 1 min and imaged using the chemiluminescence setting on an Amersham
539 680 gel imager (GE Healthcare). Blots were adjusted for brightness and contrast using GIMP (GNU Project)
540 and annotated with Illustrator (Adobe). After blotting and imaging, images were adjusted for brightness
541 and contrast and subjected to digital densitometry with ImageJ[51]. Resulting measurements were reported
542 normalized to WT Prom1 on each blot to allow comparisons between blots.
543
544 *Dynamic Light Scattering*
545 Dynamic light scattering measurements were performed using an SZ-100 Nano Particle Analyzer (Horiba).
546 EVs diluted in PBS to a volume of 1 mL were transferred to a disposable plastic cuvette (Fisher) and
547 measurements were taken using settings for polydisperse liposomes in aqueous buffer. All measurements
548 were taken at 25 °C in multiple replicates to control for instrument sampling error.
549
550 *Silver Stain*
551 EV samples were run on 7.5% SDS-PAGE Tris-Glycine gels and stained with Pierce Silver Stain for Mass
552 Spectrometry (Thermo Scientific) according to the manufacturer's protocol.
553
554 *Glycosylation Assays*
555 PNGase F (New England Biolabs) was used to remove *N*-glycan moieties from proteins under denaturing
556 conditions according to the manufacturer's instructions.
557
558 *Cryo-TEM Sample Preparation and Imaging*
559 Prom1 and Ttyh1 EVs were vitrified on 300-mesh gold Quantifoil R 1.2/1.3 + 2 nm Carbon grids (Electron
560 Microscopy Sciences). Briefly, grids were glow discharged in an EasiGlow device (Pelco) set to 5 mA, 30 s,
561 0.39 mbar, with a 15 s vacuum hold time. The grids were then treated with 5 µL of purified EVs, incubated
562 for 60 s to allow EVs to adhere to the carbon layer, then blotted with a VitroBot Mark IV (Thermo Scientific)
563 set to 22 °C, 5 s blot time, +15 blot force, 100% humidity; and plunge frozen in liquid ethane. Vitrified
564 samples were imaged on a Titan Krios microscope (Thermo Scientific) with a Falcon 4 direct electron
565 detector (Thermo Scientific) using counted detection mode, 105,000 x nominal magnification, 0.83 Å pixel
566 size, with 49-frame fractionated collection, 49.8 $e^-/Å^2$ total dose, and defocus ranging from -0.8 to -2.0
567 µm in 0.1 µm increments. Images were processed and analyzed with CryoSparc v. 4.2.1 (Structura
568 Biotechnology). Vesicles were defined and diameter (all EVs) and roundness (only EVs completely visible

569 on one micrograph) were calculated using custom scripts that extend CryoSparc, made publicly available
570 at https://github.com/tribell4310/vesicle-quantification.
571
572 *NS-TEM Sample Preparation and Imaging*
573 Formvar carbon film 400-mesh copper grids (Electron Microscopy Sciences) were glow discharged in an
574 EasiGlow device (Pelco) set to 30 mA, 30 s, 0.39 mbar, with a 15 s vacuum hold time. 5 µL of EV sample
575 was applied to a glow-discharged grid and incubated for 60 s at room temperature. The grid was then
576 blotted manually with filter paper (Whatman #43), briefly washed 3 times with 20 µL of PBS buffer,
577 blotted, washed 2 times with deionized water, blotted, washed 1 time with 1.25% (w/v) uranyl formate
578 (Electron Microscopy Sciences), and blotted. The grid was then floated for 10 s on a 20 µL of drop of 1.25%
579 uranyl formate, blotted, and allowed to air dry. Imaging was performed on a Tecnai T12 transmission
580 electron microscope (FEI) equipped with an XR16 detector (AMT) operated at an accelerating voltage of
581 120 kV, 30,000 x nominal magnification, 4.32 Å pixel size, and -1.5 µm defocus. Pixel size was manually
582 calibrated prior to image acquisition using a dedicated calibration waffle grid (Ted Pella). Data collected
583 for EV membrane area quantification was automated using SerialEM[52]. Vesicles were defined and
584 analyzed in CryoSparc (Structura Biotechnology) as described above for cryo-TEM data.
585
586 *Quantification of EV Membrane Area from NS-TEM Images*
587 NS-TEM images were collected using an automated acquisition script. The images were processed to
588 resolve membrane features from background using a custom image processing script made publicly
589 available at https://github.com/tribell4310/vesicle-quant. EV membrane area was calculated for each
590 micrograph as the fraction of pixels in the imaging area that were occupied by membrane features.
591
592 *Equilibrium Sucrose Gradient Sedimentation Analysis*
593 Linear sucrose gradients were prepared in Seton 7030 tubes using sterile-filtered 5% and 30% (w/v)
594 sucrose dissolved in PBS buffer using a Gradient Station IP (BioComp). Freshly prepared gradients were
595 loaded into an SW-41 Ti swinging bucket rotor and 200 µL of the purified EVs were layered atop
596 gradients immediately prior to centrifugation. Samples were centrifuged for 5 h, 22,000 rpm, 4 °C, then
597 fractionated into 13 fractions of 930 µL using the Gradient Station IP. Gradient fractions were analyzed
598 by SDS-PAGE and immunoblotting, then quantified as described above.
599
600 *Evolutionary Analysis of Prom and Ttyh proteins*

601 We identified sequences homologous to human Prom1 using BLAST[53] and InterPro[54]. Putative prominin
602 sequences were curated to include only sequences with five predicted transmembrane helices by
603 TMHMM[55] in a 2+2+1 pattern, containing large extracellular loops (> 300 amino acids) and 2 small
604 intracellular loops (< 25 amino acids). This broad search revealed prominin sequences across the
605 eukaryotic tree ranging from metazoans to green plants. Multiple sequence alignment was performed
606 using MAFFT[56] and phylogenetic relationships inferred using IQ-TREE with MODELFIND for evolutionary
607 model selection[57,58]. Branch supports were calculated using the approximate likelihood ratio test[59]. A
608 smaller tree was also constructed spanning only metazoan sequences, with fungi included as an outgroup
609 for rooting. For direct comparison between Prom and Ttyh sequences, homologs of human Ttyh1 were
610 identified for all species included in the prominin metazoan tree and aligned as described above. Figures
611 showing multiple sequence alignments were generated using JalView[60]. Figures showing trees were
612 generated using IcyTree[61].
613
614 Conservation of each residue within the Prom and Ttyh metazoan trees was calculated using the
615 Livingstone and Barton algorithm implemented in JalView[62]. Conservation scores were then plotted onto
616 the AlphaFold2 structure model[41] of human Prom1 or a subunit of the solved cryo-EM structure of human
617 Ttyh1[32] using PyMol (Schrödinger).
618
619 *Live Cell Fluorescence Microscopy and Analysis*
620 Confluent monoclonal HeLa cells stably expressing WT Prom1-StayGold and Prom1[W795R]-StayGold
621 were harvested, seeded onto 35 mm glass-bottom dishes (MatTek Life Sciences) coated with poly-D-lysine
622 (0.1 mg/mL) and allowed to grow overnight at 37˚C under 5% CO_2. Cells were stained with wheat germ
623 agglutinin (WGA) conjugated with AlexaFluor 647 (W32466, Thermo Fisher Scientific) at 5 µg/mL for 10
624 min at 37 ˚C, then washed twice with 1x PBS. Cells were placed in Live Cell Imaging Solution (Invitrogen)
625 prior to imaging using a Nikon A1R HD25 point scanning confocal microscope with GaAsP and PMT
626 detectors, equipped with an Apo TIRF 60x/1.49 NA objective lens and Ti2 Z-drive. Temperature, humidity,
627 and CO_2 concentrations were controlled with a Live Cell environmental chamber (Oko-Lab). Image
628 acquisition was performed in NIS-Elements (Nikon Instruments Inc.) and line-scan analysis was performed
629 using Fiji[63].
630
631 *Preparation of fluorescent cholesterol analogs*

632 BODIPY-cholesterol was procured commercially (TopFluor cholesterol, Avanti Polar Lipids) and
633 resuspended at 1 mM in ethanol. AlexaFluor647-cholesterol was synthesized from Alkyne Cholesterol and
634 AZDye 647 Azide Plus (Click Chemistry Tools) by Copper(I)-catalyzed azide-alkyne cycloaddition. Briefly, 1
635 mM AZDye 647 Azide Plus and 2 mM alkyne cholesterol (each from a 10 mM stock prepared in anhydrous
636 DMSO) were combined with 2 mM tetrakis(acetonitrile)copper(I) tetrafluoroborate (from a 40 mM stock
637 prepared in ethanol) in a 350 µL reaction brought up to volume with ethanol. The reaction was incubated
638 at 42 °C for 30 min then at 70 °C for 2 h with the reaction vessel open to allow solvent to evaporate.
639 Cholesterol was extracted from the final mixture by diluting the solution to 650 µL with PBS buffer and
640 adding 1 mL methanol and 0.5 mL chloroform. The mixture was centrifuged for 2 min at 14,000 x *g* and
641 the supernatant transferred to a clean vessel, after which 1 mL of chloroform and 2 mL of glacial acetic
642 acid were added and mixed by vortexing. The solution was then concentrated by evaporation in a SPD1010
643 SpeedVac instrument (Savant) until dried, then resuspended in 100 µL ethanol. This preparation was
644 considered to be at 5 mM labeled cholesterol (assuming 100% yield) for downstream calculations.
645
646 *Protein Expression and Purification*
647 A plasmid encoding mTagBFP2-Strep was transformed into *E. coli* BL21 (DE3) pLysS, grown at 37 °C in LB
648 media to OD_{600} 0.5-0.7, induced with 0.5 mM IPTG (Gold Biotechnology), and harvested after 3 h of
649 expression. Cells were resuspended in 25 mL per liter of culture of Buffer A (25 mM HEPES-NaOH pH 7.5,
650 500 mM NaCl, 20 mM imidazole, 0.5 mM dithiothreitol (DTT)) supplemented with 10 µM leupeptin (Sigma
651 Aldrich), 1 µM pepstatin A (Sigma Aldrich), 1 mM phenylmethylsulfonyl fluoride (Sigma Aldrich), 1 mg/mL
652 chicken egg lysozyme (Fisher), and 250 U benzonase nuclease (Sigma Aldrich); and incubated with stirring
653 for 1 h at 4 °C. Cells were then sonicated for 3 min in an ice/water bath with 5 s on / 10 s off pulses. The
654 lysate was then clarified by centrifugation in a JA-25.5 rotor (Beckman Coulter) for 45 min, 15,000 rpm,
655 4 °C. The supernatant was then loaded onto two 5-mL HisTrap columns (Cytiva) plumbed in series
656 equilibrated in Buffer A using a peristaltic pump at 1.5 mL / min flow rate. The column was washed with
657 100 mL of Buffer A and eluted with 20 mL of Buffer B (25 mM HEPES-NaOH pH 7.5, 500 mM NaCl, 300 mM
658 Imidazole, 0.5 mM DTT). The protein was found to be ~95% pure by SDS-PAGE, and the concentration of
659 the eluted material was measured using absorbance signal at 280 nm. The sample was divided into small
660 aliquots, flash frozen in liquid nitrogen and stored at -80 °C.
661
662 *Chol-IP Assays*

663 Prior to running chol-IP assays, input EVs were quantified by SDS-PAGE and immunoblotting to ensure
664 equal inputs of Prom1-Strep and/or Ttyh1-Strep in each assay. EVs were mixed 4:1 with buffer CIA (25
665 mM HEPES-NaOH pH 7.8, 150 mM NaCl, 5 mM $CaCl_2$, 5% n-dodecyl-beta-maltoside (DDM) (Anatrace)) and
666 incubated for 1 h at 4C with end-over-end rotation, protected from ambient light. During incubation,
667 0.025 µL of StrepTactinXT 4Flow resin (IBA) per condition was equilibrated with buffer CIB (25 mM HEPES-
668 NaOH pH 7.8, 150 mM NaCl, 5 mM $CaCl_2$, 1% DDM) in a single pooled reaction. mTagBFP2-Strep was added
669 to the resin at a ratio of 2 fmol mTagBFP2-Strep per 1 µL of resin, and incubated for 15 min at 4 °C with
670 end-over-end rotation, protected from ambient light. After one additional wash with buffer CIB, the resin
671 was then divided equally across low-binding 1.5 mL tubes (USA Scientific) so that each condition being
672 tested plus one negative control condition had equal inputs of BFP-labeled resin. The DDM-treated EVs
673 were then added to the appropriate resin tube and incubated for 1 h at 4 °C with end-over-end rotation,
674 protected from ambient light. Each condition was then washed twice with buffer CIB for 5 min at 4 °C with
675 end-over-end rotation, resuspended in 45 µL of buffer CIB, and stored on ice, protected from light. Each
676 condition was sequentially pipetted with a cut pipette tip onto a glass microscope slide (Fisher) and gently
677 covered with an 18 mm x 18 mm no. 1 glass cover slip (Matsunami) layered on carefully to minimize
678 trapped air bubbles. Montaged images of the resin beads were collected using an Axio Observer TIRF
679 microscope (Zeiss) in epifluorescence mode with a Prime 95B camera (Photometrics) running SlideBook
680 v. 6.0.24 software (3i). Custom scripts were then used to identify resin beads in each image using DAPI
681 (BFP) signal to both identify beads and normalize fluorescence signal in the FITC (BODIPY-cholesterol) or
682 CY5 (AlexaFluor647-cholesterol) channels. Images of all resin particles were manually reviewed to ensure
683 the exclusion of air bubbles, or other non-resin fluorescent artifacts from downstream analysis. Analysis
684 scripts have been made publicly available at https://github.com/tribell4310/bead-assay.
685
686 *Immunopurification Assays*
687 Co-immunopurification assays from EVs containing fluorescently labeled Prom1 or Pcdh21 were
688 performed as described above for the chol-IP assay, using montaged fluorescence imaging for sensitive
689 and quantitative measurements. Prom1-mScarlet was imaged using CY3 and Pcdh21-mNeonGreen using
690 FITC filter sets.
691
692 *Cholesterol depletion with methyl-beta cyclodextrin*
693 Methyl beta-cyclodextrin (mBCD) (Sigma Aldrich) was dissolved in sterile-filtered PBS buffer to a final
694 concentration of 20 mM, and a two-fold serial dilution series was prepared. For each condition (0 mM,

695 2.5 mM, 5 mM, and 10 mM mBCD), purified EVs were mixed 1:1 with the appropriate mBCD dilution and
696 incubated for 2 h at 37 °C. After the reaction was complete, the EVs were immediately re-purified over a
697 qEV2-35 nm column (Izon) as described above. Cholesterol in the purified samples was quantified using
698 Amplex Red reagent (Thermo Fisher) according to the manufacturer's protocol, with fluorescence
699 measurements taken using a SpectraMax M5 plate reader (Molecular Devices). EV morphology was
700 characterized by preparing NS-TEM grids with mBCD-treated samples and analyzing the resulting images
701 as described above.
702
703 **Data Availability**
704 Electron microscopy datasets and all biochemical data are deposited in a Zenodo repository at
705 doi:10.5281/zenodo.10034616. Custom software packages are available at
706 https://github.com/tribell4310.
707
708 **Supporting Information**
709 This article contains supporting information.
710
711 **Acknowledgments**
712 We thank D. Syau (Harvard Medical School) and members of the Chao lab for helpful feedback, and Z. Li,
713 S. Sterling, R. Walsh, M. Mayer, and S. Rawson from the Harvard Medical School Cryo-EM Center for
714 support with cryo-TEM data collection. We are grateful to Dr. Richard Bouley at the Microscopy Core of
715 the Program in Membrane Biology (PMB) at Massachusetts General Hospital for providing helpful advice
716 and equipment access for live-cell confocal microscopy. We thank the staff at the Center for Regenerative
717 Medicine (CRM) Flow Cytometry Core Facility for helpful support in cytometry sorting and analysis. This
718 work was supported by National Institutes of Health R35GM142553 (to LHC) and the Helen Hay Whitney
719 Foundation (to TAB). The content is solely the responsibility of the authors and does not necessarily
720 represent the official views of the National Institutes of Health.
721
722
723 **References**
724 1. Sharkova, M., Chow, E., Erickson, T., and Hocking, J.C. (2023). The morphological and functional
725 diversity of apical microvilli. J. Anat. *242*, 327–353. 10.1111/joa.13781.

726 2. Satir, P., and Christensen, S.T. (2007). Overview of structure and function of mammalian cilia. Annu.
727 Rev. Physiol. *69*, 377–400. 10.1146/annurev.physiol.69.040705.141236.

728 3. Brown, D.A., and London, E. (2000). Structure and Function of Sphingolipid- and Cholesterol-rich
729 Membrane Rafts*. J. Biol. Chem. *275*, 17221–17224. 10.1074/jbc.R000005200.

730 4. Corbeil, D., Marzesco, A.-M., Wilsch-Bräuninger, M., and Huttner, W.B. (2010). The intriguing links
731 between prominin-1 (CD133), cholesterol-based membrane microdomains, remodeling of apical
732 plasma membrane protrusions, extracellular membrane particles, and (neuro)epithelial cell
733 differentiation. FEBS Lett. *584*, 1659–1664. 10.1016/j.febslet.2010.01.050.

734 5. Corbeil, D., Karbanová, J., Fargeas, C.A., and Jászai, J. (2013). Prominin-1 (CD133): Molecular and
735 Cellular Features Across Species. In Prominin-1 (CD133): New Insights on Stem & Cancer Stem Cell
736 Biology Advances in Experimental Medicine and Biology., D. Corbeil, ed. (Springer), pp. 3–24.
737 10.1007/978-1-4614-5894-4_1.

738 6. Thamm, K., Šimaitė, D., Karbanová, J., Bermúdez, V., Reichert, D., Morgenstern, A., Bornhäuser, M.,
739 Huttner, W.B., Wilsch-Bräuninger, M., and Corbeil, D. (2019). Prominin-1 (CD133) modulates the
740 architecture and dynamics of microvilli. Traffic *20*, 39–60. 10.1111/tra.12618.

741 7. Yin, A.H., Miraglia, S., Zanjani, E.D., Almeida-Porada, G., Ogawa, M., Leary, A.G., Olweus, J., Kearney,
742 J., and Buck, D.W. (1997). AC133, a Novel Marker for Human Hematopoietic Stem and Progenitor
743 Cells. Blood *90*, 5002–5012. 10.1182/blood.V90.12.5002.

744 8. Miraglia, S., Godfrey, W., Yin, A.H., Atkins, K., Warnke, R., Holden, J.T., Bray, R.A., Waller, E.K., and
745 Buck, D.W. (1997). A Novel Five-Transmembrane Hematopoietic Stem Cell Antigen: Isolation,
746 Characterization, and Molecular Cloning. Blood *90*, 5013–5021. 10.1182/blood.V90.12.5013.

747 9. Corbeil, D., Röper, K., Weigmann, A., and Huttner, W.B. (1998). AC133 Hematopoietic Stem Cell
748 Antigen: Human Homologue of Mouse Kidney Prominin or Distinct Member of a Novel Protein
749 Family? Blood *91*, 2625–2626. 10.1182/blood.V91.7.2625.

750 10. Kemper, K., Tol, M.J.P.M., and Medema, J.P. (2010). Mouse Tissues Express Multiple Splice
751 Variants of Prominin-1. PLOS ONE *5*, e12325. 10.1371/journal.pone.0012325.

752 11. Mak, A.B., Nixon, A.M.L., Kittanakom, S., Stewart, J.M., Chen, G.I., Curak, J., Gingras, A.-C.,
753 Mazitschek, R., Neel, B.G., Stagljar, I., et al. (2012). Regulation of CD133 by HDAC6 Promotes β-
754 Catenin Signaling to Suppress Cancer Cell Differentiation. Cell Rep. *2*, 951–963.
755 10.1016/j.celrep.2012.09.016.

756 12. Yang, Z., Chen, Y., Lillo, C., Chien, J., Yu, Z., Michaelides, M., Klein, M., Howes, K.A., Li, Y.,
757 Kaminoh, Y., et al. (2008). Mutant prominin 1 found in patients with macular degeneration disrupts
758 photoreceptor disk morphogenesis in mice. J. Clin. Invest. *118*, 2908–2916. 10.1172/JCI35891.

759 13. Burgoyne, T., Meschede, I.P., Burden, J.J., Bailly, M., Seabra, M.C., and Futter, C.E. (2015). Rod
760 disc renewal occurs by evagination of the ciliary plasma membrane that makes cadherin-based
761 contacts with the inner segment. Proc. Natl. Acad. Sci. *112*, 15922–15927.
762 10.1073/pnas.1509285113.

763 14. Rattner, A., Smallwood, P.M., Williams, J., Cooke, C., Savchenko, A., Lyubarsky, A., Pugh, E.N.,
764 and Nathans, J. (2001). A Photoreceptor-Specific Cadherin Is Essential for the Structural Integrity of
765 the Outer Segment and for Photoreceptor Survival. Neuron *32*, 775–786. 10.1016/S0896-
766 6273(01)00531-1.

767 15. Zacchigna, S., Oh, H., Wilsch-Bräuninger, M., Missol-Kolka, E., Jászai, J., Jansen, S., Tanimoto, N.,
768 Tonagel, F., Seeliger, M., Huttner, W.B., et al. (2009). Loss of the Cholesterol-Binding Protein
769 Prominin-1/CD133 Causes Disk Dysmorphogenesis and Photoreceptor Degeneration. J. Neurosci. *29*,
770 2297–2308. 10.1523/JNEUROSCI.2034-08.2009.

771 16. Eidinger, O., Leibu, R., Newman, H., Rizel, L., Perlman, I., and Ben-Yosef, T. (2015). An intronic
772 deletion in the PROM1 gene leads to autosomal recessive cone-rod dystrophy. Mol. Vis. *21*, 1295–
773 1306.

774 17. Liang, J., She, X., Chen, J., Zhai, Y., Liu, Y., Zheng, K., Gong, Y., Zhu, H., Luo, X., and Sun, X. (2019).
775 Identification of novel PROM1 mutations responsible for autosomal recessive maculopathy with rod-
776 cone dystrophy. Graefes Arch. Clin. Exp. Ophthalmol. *257*, 619–628. 10.1007/s00417-018-04206-w.

777 18. Maw, M.A., Corbeil, D., Koch, J., Hellwig, A., Wilson-Wheeler, J.C., Bridges, R.J.,
778 Kumaramanickavel, G., John, S., Nancarrow, D., Röper, K., et al. (2000). A frameshift mutation in
779 prominin (mouse)-like 1 causes human retinal degeneration. Hum. Mol. Genet. *9*, 27–34.
780 10.1093/hmg/9.1.27.

781 19. Fargeas, C.A. (2013). Prominin-2 and Other Relatives of CD133. In Prominin-1 (CD133): New
782 Insights on Stem & Cancer Stem Cell Biology Advances in Experimental Medicine and Biology., D.
783 Corbeil, ed. (Springer), pp. 25–40. 10.1007/978-1-4614-5894-4_2.

784 20. Hori, A., Nishide, K., Yasukuni, Y., Haga, K., Kakuta, W., Ishikawa, Y., Hayes, M.J., Ohnuma, S.,
785 Kiyonari, H., Kimura, K., et al. (2019). Prominin-1 Modulates Rho/ROCK-Mediated Membrane
786 Morphology and Calcium-Dependent Intracellular Chloride Flux. Sci. Rep. *9*, 15911. 10.1038/s41598-
787 019-52040-9.

788 21. Röper, K., Corbeil, D., and Huttner, W.B. (2000). Retention of prominin in microvilli reveals
789 distinct cholesterol-based lipid micro-domains in the apical plasma membrane. Nat. Cell Biol. *2*, 582–
790 592. 10.1038/35023524.

791 22. Marzesco, A.-M., Janich, P., Wilsch-Bräuninger, M., Dubreuil, V., Langenfeld, K., Corbeil, D., and
792 Huttner, W.B. (2005). Release of extracellular membrane particles carrying the stem cell marker
793 prominin-1 (CD133) from neural progenitors and other epithelial cells. J. Cell Sci. *118*, 2849–2858.
794 10.1242/jcs.02439.

795 23. Wood, C.R., and Rosenbaum, J.L. (2015). Ciliary ectosomes: transmissions from the cell's
796 antenna. Trends Cell Biol. *25*, 276–285. 10.1016/j.tcb.2014.12.008.

797 24. Dubreuil, V., Marzesco, A.-M., Corbeil, D., Huttner, W.B., and Wilsch-Bräuninger, M. (2007).
798 Midbody and primary cilium of neural progenitors release extracellular membrane particles enriched
799 in the stem cell marker prominin-1. J. Cell Biol. *176*, 483–495. 10.1083/jcb.200608137.

800 25. Hurbain, I., Macé, A.-S., Romao, M., Prince, E., Sengmanivong, L., Ruel, L., Basto, R., Thérond,
801 P.P., Raposo, G., and D'Angelo, G. (2022). Microvilli-derived extracellular vesicles carry Hedgehog
802 morphogenic signals for Drosophila wing imaginal disc development. Curr. Biol. *32*, 361-373.e6.
803 10.1016/j.cub.2021.11.023.

804 26. Campbell, H.D., Kamei, M., Claudianos, C., Woollatt, E., Sutherland, G.R., Suzuki, Y., Hida, M.,
805 Sugano, S., and Young, I.G. (2000). Human and Mouse Homologues of the Drosophila melanogaster
806 tweety (tty) Gene: A Novel Gene Family Encoding Predicted Transmembrane Proteins. Genomics *68*,
807 89–92. 10.1006/geno.2000.6259.

808 27. Matthews, C.A., Shaw, J.E., Hooper, J.A., Young, I.G., Crouch, M.F., and Campbell, H.D. (2007).
809 Expression and evolution of the mammalian brain gene Ttyh1. J. Neurochem. *100*, 693–707.
810 10.1111/j.1471-4159.2006.04237.x.

811 28. Halleran, A.D., Sehdev, M., Rabe, B.A., Huyck, R.W., Williams, C.C., and Saha, M.S. (2015).
812 Characterization of tweety gene (ttyh1-3) expression in Xenopus laevis during embryonic
813 development. Gene Expr. Patterns *17*, 38–44. 10.1016/j.gep.2014.12.002.

814 29. Bae, Y., Kim, A., Cho, C.-H., Kim, D., Jung, H.-G., Kim, S.-S., Yoo, J., Park, J.-Y., and Hwang, E.M.
815 (2019). TTYH1 and TTYH2 Serve as LRRC8A-Independent Volume-Regulated Anion Channels in Cancer
816 Cells. Cells *8*, 562. 10.3390/cells8060562.

817 30. Han, Y.-E., Kwon, J., Won, J., An, H., Jang, M.W., Woo, J., Lee, J.S., Park, M.G., Yoon, B.-E., Lee,
818 S.E., et al. (2019). Tweety-homolog (Ttyh) Family Encodes the Pore-forming Subunits of the Swelling-
819 dependent Volume-regulated Anion Channel (VRACswell) in the Brain. Exp. Neurobiol. *28*, 183–215.
820 10.5607/en.2019.28.2.183.

821 31. Li, B., Hoel, C.M., and Brohawn, S.G. (2021). Structures of Tweety Homolog Proteins TTYH2 and
822 TTYH3 reveal a Ca2+-dependent switch from intra- to inter-membrane dimerization
823 10.1101/2021.08.15.456437.

824 32. Sukalskaia, A., Straub, M.S., Deneka, D., Sawicka, M., and Dutzler, R. (2021). Cryo-EM structures
825 of the TTYH family reveal a novel architecture for lipid interactions. Nat. Commun. *12*, 4893.
826 10.1038/s41467-021-25106-4.

827 33. Melvin, E., Kalaninová, Z., Shlush, E., Man, P., Giladi, M., and Haitin, Y. (2022). TTYH family
828 members form tetrameric complexes at the cell membrane. Commun. Biol. *5*, 1–11. 10.1038/s42003-
829 022-03862-3.

830 34. Jung, E., Osswald, M., Blaes, J., Wiestler, B., Sahm, F., Schmenger, T., Solecki, G., Deumelandt, K.,
831 Kurz, F.T., Xie, R., et al. (2017). Tweety-Homolog 1 Drives Brain Colonization of Gliomas. J. Neurosci.
832 *37*, 6837–6850. 10.1523/JNEUROSCI.3532-16.2017.

833 35. Stefaniuk, M., Swiech, L., Dzwonek, J., and Lukasiuk, K. (2010). Expression of Ttyh1, a member of
834 the Tweety family in neurons in vitro and in vivo and its potential role in brain pathology. J.
835 Neurochem. *115*, 1183–1194. 10.1111/j.1471-4159.2010.07023.x.

836 36. Wiernasz, E., Kaliszewska, A., Brutkowski, W., Bednarczyk, J., Gorniak, M., Kaza, B., and Lukasiuk,
837 K. (2014). Ttyh1 Protein is Expressed in Glia In Vitro and Shows Elevated Expression in Activated

838 Astrocytes Following Status Epilepticus. Neurochem. Res. *39*, 2516–2526. 10.1007/s11064-014-1455-
839 3.

840 37. Kemper, K., Sprick, M.R., Bree, M. de, Scopelliti, A., Vermeulen, L., Hoek, M., Zeilstra, J., Pals,
841 S.T., Mehmet, H., Stassi, G., et al. (2010). The AC133 Epitope, but not the CD133 Protein, Is Lost upon
842 Cancer Stem Cell Differentiation. Cancer Res. *70*, 719–729. 10.1158/0008-5472.CAN-09-1820.

843 38. Huttner, W.B., Schiebler, W., Greengard, P., and De Camilli, P. (1983). Synapsin I (protein I), a
844 nerve terminal-specific phosphoprotein. III. Its association with synaptic vesicles studied in a highly
845 purified synaptic vesicle preparation. J. Cell Biol. *96*, 1374–1388. 10.1083/jcb.96.5.1374.

846 39. Fantini, J., and Barrantes, F.J. (2013). How cholesterol interacts with membrane proteins: an
847 exploration of cholesterol-binding sites including CRAC, CARC, and tilted domains. Front. Physiol. *4*.
848 10.3389/fphys.2013.00031.

849 40. Boulanger-Scemama, E., El Shamieh, S., Démontant, V., Condroyer, C., Antonio, A., Michiels, C.,
850 Boyard, F., Saraiva, J.-P., Letexier, M., Souied, E., et al. (2015). Next-generation sequencing applied to
851 a large French cone and cone-rod dystrophy cohort: mutation spectrum and new genotype-
852 phenotype correlation. Orphanet J. Rare Dis. *10*, 85. 10.1186/s13023-015-0300-3.

853 41. Jumper, J., Evans, R., Pritzel, A., Green, T., Figurnov, M., Ronneberger, O., Tunyasuvunakool, K.,
854 Bates, R., Žídek, A., Potapenko, A., et al. (2021). Highly accurate protein structure prediction with
855 AlphaFold. Nature *596*, 583–589. 10.1038/s41586-021-03819-2.

856 42. Derganc, J., and Čopič, A. (2016). Membrane bending by protein crowding is affected by protein
857 lateral confinement. Biochim. Biophys. Acta BBA - Biomembr. *1858*, 1152–1159.
858 10.1016/j.bbamem.2016.03.009.

859 43. Zidovetzki, R., and Levitan, I. (2007). Use of cyclodextrins to manipulate plasma membrane
860 cholesterol content: Evidence, misconceptions and control strategies. Biochim. Biophys. Acta BBA -
861 Biomembr. *1768*, 1311–1324. 10.1016/j.bbamem.2007.03.026.

862 44. Salinas, R.Y., Pearring, J.N., Ding, J.-D., Spencer, W.J., Hao, Y., and Arshavsky, V.Y. (2017).
863 Photoreceptor discs form through peripherin-dependent suppression of ciliary ectosome release. J.
864 Cell Biol. *216*, 1489–1499. 10.1083/jcb.201608081.

865 45. Lorent, J.H., Levental, K.R., Ganesan, L., Rivera-Longsworth, G., Sezgin, E., Doktorova, M., Lyman,
866 E., and Levental, I. (2020). Plasma membranes are asymmetric in lipid unsaturation, packing and
867 protein shape. Nat. Chem. Biol. *16*, 644–652. 10.1038/s41589-020-0529-6.

868 46. Ridsdale, A., Denis, M., Gougeon, P.-Y., Ngsee, J.K., Presley, J.F., and Zha, X. (2006). Cholesterol
869 Is Required for Efficient Endoplasmic Reticulum-to-Golgi Transport of Secretory Membrane Proteins.
870 Mol. Biol. Cell *17*, 1593–1605. 10.1091/mbc.e05-02-0100.

871 47. Stüven, E., Porat, A., Shimron, F., Fass, E., Kaloyanova, D., Brügger, B., Wieland, F.T., Elazar, Z.,
872 and Helms, J.B. (2003). Intra-Golgi Protein Transport Depends on a Cholesterol Balance in the Lipid
873 Membrane*. J. Biol. Chem. *278*, 53112–53122. 10.1074/jbc.M300402200.

874 48. Fargeas, C.A., Huttner, W.B., and Corbeil, D. (2007). Nomenclature of prominin-1 (CD133) splice
875 variants – an update. Tissue Antigens *69*, 602–606. 10.1111/j.1399-0039.2007.00825.x.

876 49. Elegheert, J., Behiels, E., Bishop, B., Scott, S., Woolley, R.E., Griffiths, S.C., Byrne, E.F.X., Chang,
877 V.T., Stuart, D.I., Jones, E.Y., et al. (2018). Lentiviral transduction of mammalian cells for fast, scalable
878 and high-level production of soluble and membrane proteins. Nat. Protoc. *13*, 2991–3017.
879 10.1038/s41596-018-0075-9.

880 50. Kutner, R.H., Zhang, X.-Y., and Reiser, J. (2009). Production, concentration and titration of
881 pseudotyped HIV-1-based lentiviral vectors. Nat. Protoc. *4*, 495–505. 10.1038/nprot.2009.22.

882 51. Schneider, C.A., Rasband, W.S., and Eliceiri, K.W. (2012). NIH Image to ImageJ: 25 years of image
883 analysis. Nat. Methods *9*, 671–675. 10.1038/nmeth.2089.

884 52. Mastronarde, D.N. (2005). Automated electron microscope tomography using robust prediction
885 of specimen movements. J. Struct. Biol. *152*, 36–51. 10.1016/j.jsb.2005.07.007.

886 53. Sayers, E.W., Bolton, E.E., Brister, J.R., Canese, K., Chan, J., Comeau, D.C., Connor, R., Funk, K.,
887 Kelly, C., Kim, S., et al. (2022). Database resources of the national center for biotechnology
888 information. Nucleic Acids Res. *50*, D20–D26. 10.1093/nar/gkab1112.

889 54. Paysan-Lafosse, T., Blum, M., Chuguransky, S., Grego, T., Pinto, B.L., Salazar, G.A., Bileschi, M.L.,
890 Bork, P., Bridge, A., Colwell, L., et al. (2023). InterPro in 2022. Nucleic Acids Res. *51*, D418–D427.
891 10.1093/nar/gkac993.

892 55. Sonnhammer, E.L., von Heijne, G., and Krogh, A. (1998). A hidden Markov model for predicting
893 transmembrane helices in protein sequences. Proc. Int. Conf. Intell. Syst. Mol. Biol. *6*, 175–182.

894 56. Katoh, K., Misawa, K., Kuma, K., and Miyata, T. (2002). MAFFT: a novel method for rapid multiple
895 sequence alignment based on fast Fourier transform. Nucleic Acids Res. *30*, 3059–3066.
896 10.1093/nar/gkf436.

897 57. Minh, B.Q., Schmidt, H.A., Chernomor, O., Schrempf, D., Woodhams, M.D., von Haeseler, A., and
898 Lanfear, R. (2020). IQ-TREE 2: New Models and Efficient Methods for Phylogenetic Inference in the
899 Genomic Era. Mol. Biol. Evol. *37*, 1530–1534. 10.1093/molbev/msaa015.

900 58. Kalyaanamoorthy, S., Minh, B.Q., Wong, T.K.F., von Haeseler, A., and Jermiin, L.S. (2017).
901 ModelFinder: fast model selection for accurate phylogenetic estimates. Nat. Methods *14*, 587–589.
902 10.1038/nmeth.4285.

903 59. Anisimova, M., and Gascuel, O. (2006). Approximate Likelihood-Ratio Test for Branches: A Fast,
904 Accurate, and Powerful Alternative. Syst. Biol. *55*, 539–552. 10.1080/10635150600755453.

905 60. Clamp, M., Cuff, J., Searle, S.M., and Barton, G.J. (2004). The Jalview Java alignment editor.
906 Bioinformatics *20*, 426–427. 10.1093/bioinformatics/btg430.

907 61. Vaughan, T.G. (2017). IcyTree: rapid browser-based visualization for phylogenetic trees and
908 networks. Bioinformatics *33*, 2392–2394. 10.1093/bioinformatics/btx155.

909 62. Livingstone, C.D., and Barton, G.J. (1993). Protein sequence alignments: a strategy for the
910 hierarchical analysis of residue conservation. Bioinformatics *9*, 745–756.
911 10.1093/bioinformatics/9.6.745.

912 63. Schindelin, J., Arganda-Carreras, I., Frise, E., Kaynig, V., Longair, M., Pietzsch, T., Preibisch, S.,
913 Rueden, C., Saalfeld, S., Schmid, B., et al. (2012). Fiji: an open-source platform for biological-image
914 analysis. Nat. Methods *9*, 676–682. 10.1038/nmeth.2019.

915